

Discovery of non-random spatial distribution of impacts in the Stardust cometary collector

Andrew J. Westphal^{1*}, Ronald K. Bastien¹⁰, Janet Borg², John Bridges³,
Donald E. Brownlee⁴,
Mark J. Burchell¹⁶,
Andrew F. Cheng⁵, Benton C. Clark⁶, Zahia Djouadi²,
Christine Floss¹³, Ian Franchi³, Zack Gainsforth¹, Giles Graham⁷,
Simon F. Green³, Philipp R. Heck⁸, Mihaly Horányi⁹,
Peter Hoppe⁸, Friedrich P. Hörz¹⁰, Joachim Huth⁸,
Anton Kearsley¹¹, Hugues Leroux¹¹, Kuljeet Marhas¹³, Keiko Nakamura¹⁰,
Scott A. Sandford¹², Thomas H. See¹⁰,
Frank Stadermann¹³, Samuel Tsitritin¹, Peter Tsou¹⁴,
Jack L. Warren¹⁰, Penelope J. Wozniakiewicz^{11,15},
Michael E. Zolensky¹⁰

¹ Space Sciences Laboratory, University of California at Berkeley, Berkeley CA 94720, USA

² IAS Orsay, Bâtiment 121, Campus 91405 Orsay Cedex, France

³ PSSRI, Open University, Milton Keynes MK7 6AA, UK

⁴ Astronomy Department, University of Washington, Seattle, WA 98195, USA

⁵ Johns Hopkins University Applied Physics Laboratory, 11100 Johns Hopkins Road, Laurel, MD 20723 USA

⁶ Lockheed Martin Corporation, Littleton, CO, USA

⁷ IGPP, Lawrence Livermore National Laboratory, 7000 East Avenue, L-413, Livermore, CA 94550, USA

⁸ Max-Planck-Institut für Chemie, P. O. Box 3060, D-55020 Mainz, Germany

⁹ Laboratory for Atmospheric and Space Physics & Department of Physics, University of Colorado, Boulder, CO 80309-0392, USA

¹⁰ KT NASA Johnson Space Center, Houston, TX 77058, USA

¹¹ IARC, Department of Mineralogy, The Natural History Museum, London SW7 5BD, UK

¹² Astrophysics Branch, Mail Stop 245-6, NASA-Ames Research Center, Moffett Field, CA 94035 USA

¹³ Laboratory for Space Sciences and Physics Department, Washington University, St. Louis MO 63130, USA

¹⁴ Jet Propulsion Laboratory, California Institute of Technology, Pasadena, CA 91109 USA

¹⁵ IARC, Department of Earth Science and Engineering, Imperial College London, South Kensington Campus, London SW11 3RA, UK

¹⁶ School of Physical Sciences, Room 119, Ingram Building, University of Kent, Canterbury, Kent CT2 7NH, UK

¹⁷ LSPES, Lille II, France

*To whom correspondence should be addressed; E-mail: westphal@ssl.berkeley.edu.

We report the discovery that impacts in the Stardust cometary collector are not distributed randomly in the collecting media, but appear to be clustered on scales smaller than ~ 10 cm. We also report the discovery of at least two populations of oblique tracks. We evaluated several hypotheses that could explain the observations. No hypothesis was consistent with all the observations, but the preponderance of evidence points toward at least one impact on the central Whipple shield of the spacecraft as the origin of both clustering and low-angle oblique tracks. High-angle oblique tracks unambiguously originate from a non-cometary impact on the spacecraft bus just forward of the collector.

On 2 January 2004, the Stardust spacecraft encountered the comet 81P/Wild2 at 1.8 AU from the sun at a relative speed of 6.1 km sec^{-1} (1). The distance of closest approach was 236 km, on the sunward side. An on-board dust flux monitor (DFMI) recorded thousands of impacts during two main collection periods of comparable fluence (5). The first period was ~ 3 minutes long and was centered on the time of closest approach. The second collection was 1.5 minutes long and began about 11 minutes after closest approach. An array of aerogel tiles and aluminum foils was deployed during the encounter to capture cometary particles. The Stardust cometary collector comprised 132 aerogel tiles and 240 aluminum foils, with total collecting areas of $\sim 1050 \text{ cm}^2$ and $\sim 153 \text{ cm}^2$ respectively (4). On 15 January 2006 this collector returned to Earth and was successfully recovered. During the Stardust Preliminary Examination, we optically scanned 132 tiles and 240 foils from which the data discussed here originate. In addition, we did systematic high-magnification surveys by Scanning Electron Microscopy on eleven foils.

The organization of this paper is as follows. In section 1, we report our observations of the spatial distributions of impacts in the Stardust collector, and our statistical analysis of these distributions. In section 2, we report the trajectory measurements of tracks in five aerogel tiles. In section 3, we summarize the results of the chemical and mineralogical analyses of residues in craters and tracks. In section 4, we compare the dust fluence measurements derived from the DFMI instrument and from measurements of crater diameters in Stardust Al foils. In section 5, we discuss the consistency of several hypotheses with the observations. In section 6, we summarize and conclude.

1 Spatial distributions of impacts in the Stardust collector

Observations

During the course of the preliminary examination, we did surveys to determine the spatial distribution of impacts in the aerogel and foils. These surveys resulted in four sets of data: complete low-magnification photographic surveys of impacts in aerogel and foils on the entire cometary tray, a high-magnification surveys of four aerogel tiles, all by optical microscopy, and very high-magnification surveys of eleven aluminum foils by scanning electron microscopy. We also measured the trajectories of 61 tracks in five aerogel tiles. Independently of these observations, we considered *in situ* observations of dust impacts during the cometary encounter by the DFMI instrument, and measurements of the compositions of track and crater residues. Here we summarize the observations.

Low-magnification survey of impacts in aerogel and foils

Using a low-magnification microscope in reflection mode, three of us (THS, RKB and JLW) recorded digital images of every aerogel tile in the cometary collector, and assembled these images into photomosaics. In order to maintain a consistent selection bias, three of us (PJW, FPH, and THS) surveyed these images and recorded sizes and coordinates of 257 impact tracks. The threshold detection diameter for aerogel tracks was 100-500 μm .

Independently, two of us (FPH, THS and JLW) surveyed the foils for craters using the same microscope, recording the sizes and positions of each crater. In all, 64 craters $>20 \mu\text{m}$ were found. Because of the very different visibilities of impacts in the two media, the detection thresholds are quite different, and we did not combine the two datasets. In the analysis described below, we considered only impacts into the aerogel tiles.

Whole tile analysis of normal tracks

Four tiles that were extracted from the Stardust tray were completely scanned by three of us (AJW, SS, and ST) by high-magnification microscopy with transmitted illumination. Transmitted illumination enabled orientation to be estimated. These tiles (9, 27, 44 and 115) contained 4, 15, 8 and 9 apparently normal-incidence ($<\sim 10^\circ$) tracks, respectively. Tile 9 also contained a large number (~ 100) of very small tracks which entered the aerogel at a significant angle ($\sim 8 - 10^\circ$) to the tile normal.

foil	Group	area scanned (mm ²)	craters count (> 350nm)	fluence (mm ⁻²) (> 350nm)
20W1	Borg <i>et al.</i>	18.3	***66?	***3.7 ± 0.5 ?
68W		18.3	***15?	***0.82 ± 0.21
92N		41	3	0.07 ^{+0.07} _{-0.04}
114N		54	3	0.06 ± ^{+0.05} _{-0.03}
43N		56	2	0.036 ^{+0.047} _{-0.023}
100N	Graham <i>et al.</i>	5	9	1.8 ± 0.6
8N	Green <i>et al.</i>	54.4	*** 81?	***1.49 ± 0.16?
20W2		12.4	0	< 0.15
37N	Hoppe <i>et al.</i>	1.42	34	24 ± 4
44W		5.5	10	2.0 ± 0.6
52N		9.0	101	11.2 ± 1.1
126W		5.2	1	0.19 ^{+0.44} _{-0.16}
44N	Stadermann <i>et al.</i>	8.2	26	3.1 ± 0.6

Table 1: Summary of small crater observations. Confidence limits for small statistics were calculated using the tables of Gehrels (10).

Small craters in foils

As part of the “cratering” Preliminary Examination subteam effort, several of us (the Mainz, Orsay, OU, Livermore, and Washington University groups) surveyed, using SEM, all removed foils at a magnification allowing identification of all craters down to a size of 1 μm . In a second step, randomly-selected regions of eleven foils were scanned by high-magnification SEM. First results are summarised in Hörz *et al.* (9) and will be presented in more detail in Green *et al.* and Kearsley *et al.* (in preparation).

In Table 1 we report the crater surface densities as derived from these surveys. The crater density varies between foils by more than a factor of 700. In Fig. 1 we show a graphical summary of the survey data.

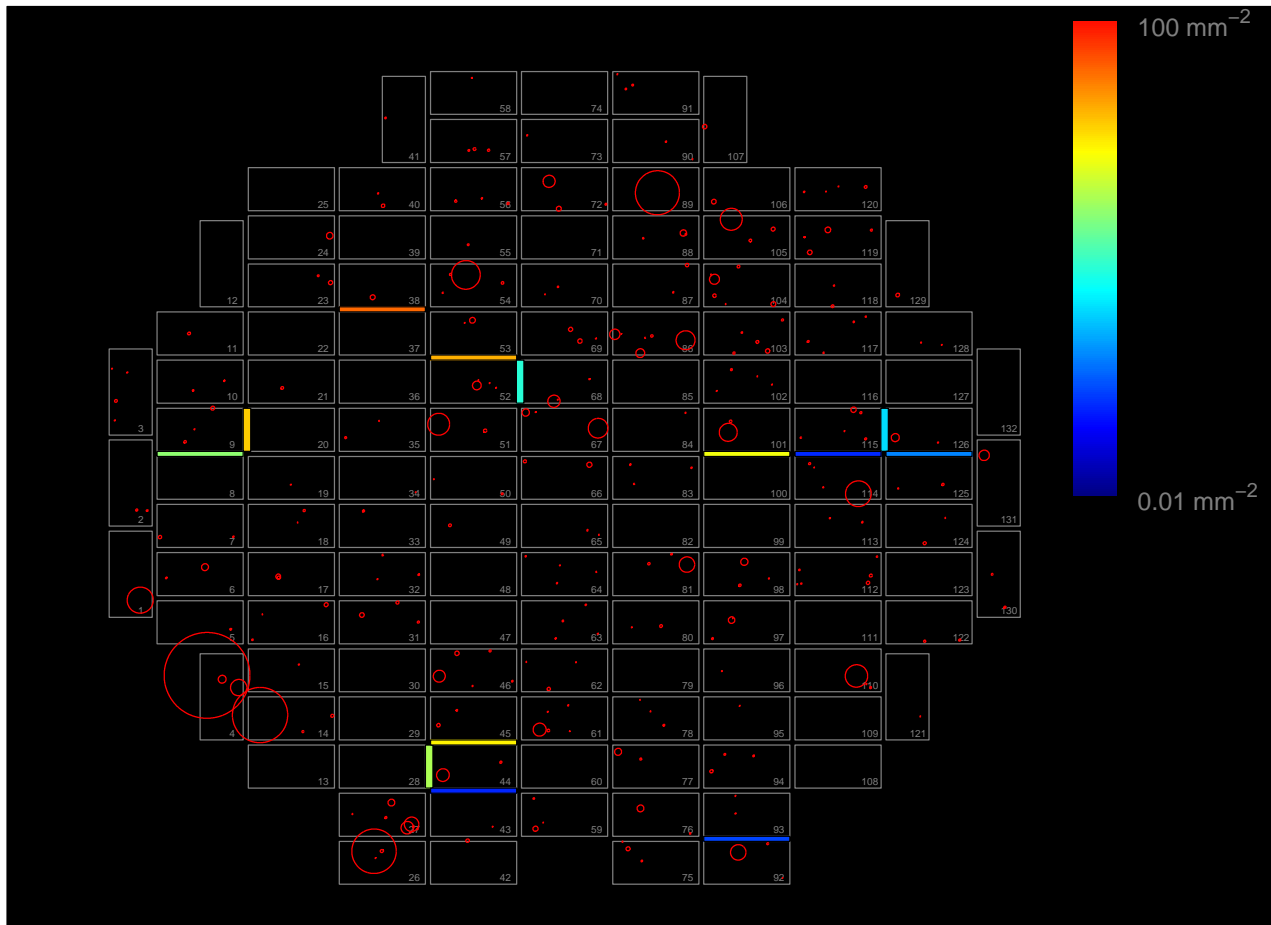


Figure 1: Schematic diagram of the Stardust cometary collector. Tracks in aerogel are shown, with the diameters of the circles proportional to the maximum throat diameter of the particle track. Crater densities in foils are also shown in false-color, according to the legend at right. The numbers are the official tile numbers. 'N' and 'W' foils are adjacent (north and west) of the aerogel cells with the same name. Aerogel tiles measure 2cm \times 4cm.

Clustering analysis

Whole-collector analysis of tracks in aerogel

A casual inspection of Fig. 1 shows hints of non-random distributions. For example, the two largest tracks in the collection are about 30 mm apart. However, such a coincidence — considered in isolation — is reasonably probable, about 2%.

In order to test rigorously for randomness in the spatial distribution of tracks in aerogel, we considered three statistical tools. The choice of tool was motivated by the nature of the question that we chose to ask: is there a small population of tightly-clustered impacts superimposed on a larger randomly-distributed population? (Are there “weak clusters”?)

The first is a tool commonly used in cosmology, the two-point correlation function (2PCF) (2). The 2PCF, $\hat{\xi}$, is a measure of the excess probability of finding neighbors as a function of separation distance r :

$$\hat{\xi}(r, \Delta) = \frac{\sum_{\text{pairs}} \phi(d_{\text{obs}}, r, \Delta)}{\sum_{\text{pairs}} \phi(d_{\text{MC}}, r, \Delta)} - 1$$

where $\phi(d, r, \Delta) = 1$ if $r < d < r + \Delta$, otherwise 0. Here d_{obs} are the separation distances of the $N(N-1)/2$ unique pairs among the N impacts in the dataset; d_{MC} are the pair-wise separation distances of randomly-placed impacts over the same fiducial area, and Δ is the bin width.

Our second statistical tool was a single statistic $\hat{\zeta}$. ζ is defined as

$$\zeta = \log \sum_{\text{pairs}} \frac{1}{d_{\text{pair}}^2},$$

where d_{pair} is the separation distance of each pair, and the sum is taken over the $N(N-1)/2$ unique pairs among the N tracks in the fiducial region. $\hat{\zeta} = \zeta - \langle \zeta_{\text{MC}} \rangle$, where $\langle \zeta_{\text{MC}} \rangle$ is the average value of ζ for a large ensemble of Monte Carlo simulations of N randomly positioned events on the tile. $\langle \zeta_{\text{MC}} \rangle$ and the error bars were determined by running 10 000 Monte Carlo simulations.

Finally, we considered a standard technique in cratering analysis, Mean Nearest Neighbor Analysis (21).

We evaluated all three techniques (2PCF, $\hat{\zeta}$ and MNNA) using a randomly-generated dataset consisting of 232

tracks randomly distributed over the tray and with an additional 25 tracks randomly distributed within a quarter of one tile. We found that 2PCF and $\hat{\xi}$ both showed very highly significant deviations from random distributions, but that, somewhat surprisingly, MNNA was insensitive to the presence of the cluster, showing $< 1\sigma$ deviation from random. We concluded that MNNA is not well-suited for testing for weak clustering analysis.

Figure 2 shows the 2PCF for the distribution of tracks in aerogel. The error bars were determined using 10 000 Monte Carlo simulations of randomly-distributed tracks in the aerogel tiles in the tray. A random distribution gives, within errors, a flat distribution at $\hat{\xi} = 0$. The 2PCF shows a significant (2.8σ) excess probability of about 10%, at the smallest scale (less than ~ 50 mm), with weaker evidence of a deficit at the scales larger than ~ 20 cm.

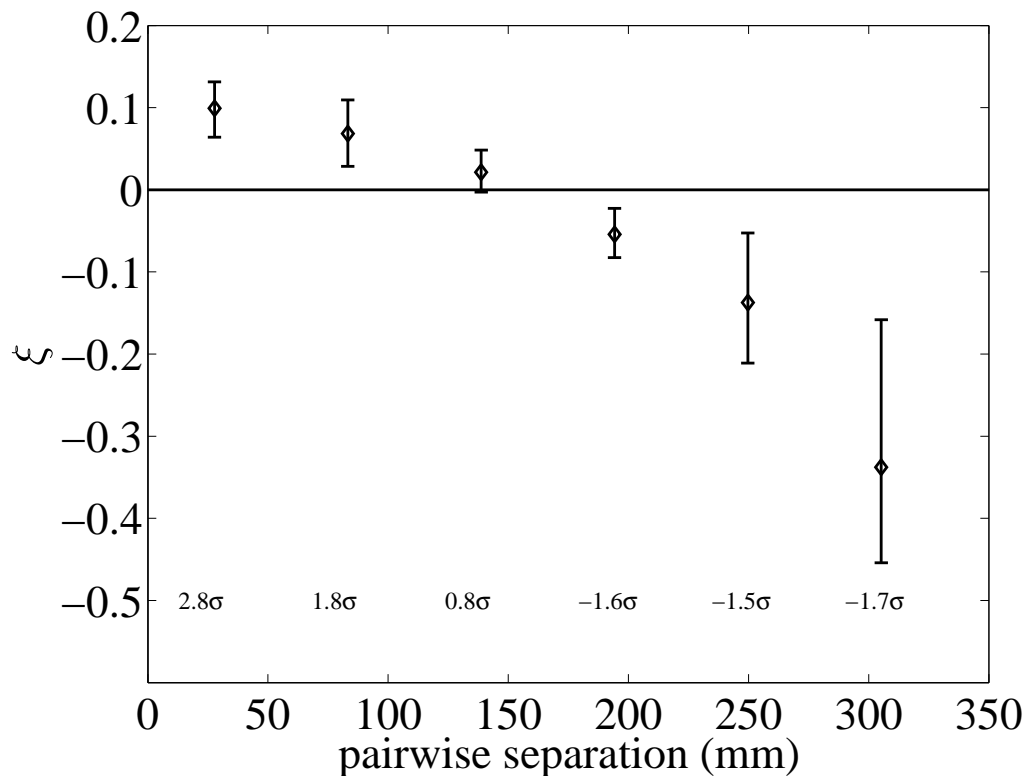


Figure 2: The two-point correlation function $\hat{\xi}$ plotted versus track separation. The statistical significance of the departure from random ($\hat{\xi} = 0$) is given for each point.

To test whether the clustering might be due to a specific size range, we progressively removed small tracks from the dataset. We chose to look at the bin with the largest $\hat{\xi}$ value, $\hat{\xi}_1$, in the bin centered on 30 mm in Fig. 2.

We divided the dataset into deciles, then removed first the smallest 10%, the smallest 20%, and so on. The largest statistical excess (2.7σ) in the 2PCF is shown by the entire dataset, but the excess does not appear to decrease significantly with increasing minimum particle size.

We also evaluated the dataset using the $\hat{\zeta}$ statistic. Again, we removed the smallest tracks in deciles. The results are shown in Fig. 3. We find evidence that the smallest 10% of tracks are responsible for the statistical excess (2.4σ) in $\hat{\zeta}$. There is also a marginal statistical excess (2.0σ) for tracks larger than $\sim 300 \mu\text{m}$.

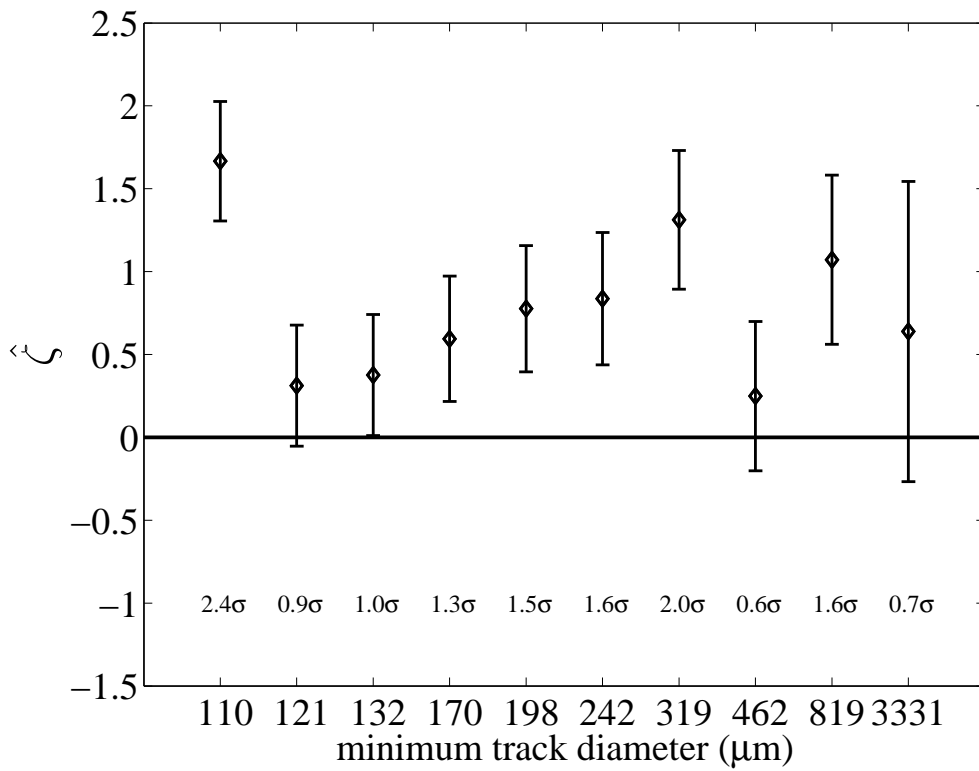


Figure 3: $\hat{\zeta}$ versus minimum particle size.

Whole-tile analysis of tracks in aerogel

The tiles that we analyzed, 9, 27, 44 and 115, contained, at most, 15 normal-incidence tracks. For such small track statistics, the 2PCF is not useful as a statistical measure, so we used the $\hat{\zeta}$ statistic only.

Only one of the four tiles, tile 27 (Fig. ??), showed significant evidence of clustering. In Fig. 4 we show a

map of the track locations in tile 27. This tile contains two large, nearly identical impacts, that are only ~ 3 mm apart, near three other tracks. However, the tracks analyzed in tile 27 include both large and small particles. As mentioned above, tile 9 contained numerous off-normal tracks. These tracks were not included in the clustering analysis described here. The situation with tile 27 is ambiguous — unfortunately, the tracks were extracted for analysis before their trajectories could be analyzed.

(it is surprising that the tile 27 shown on fig 8 is surrounded by Al foils, 2 of which 27N and 43W were analysed, showing respectively 2 and 5 craters no clustering in these foils). Could there be a discussion of comparison of clustering data in tiles and nearby foils ? – Janet)

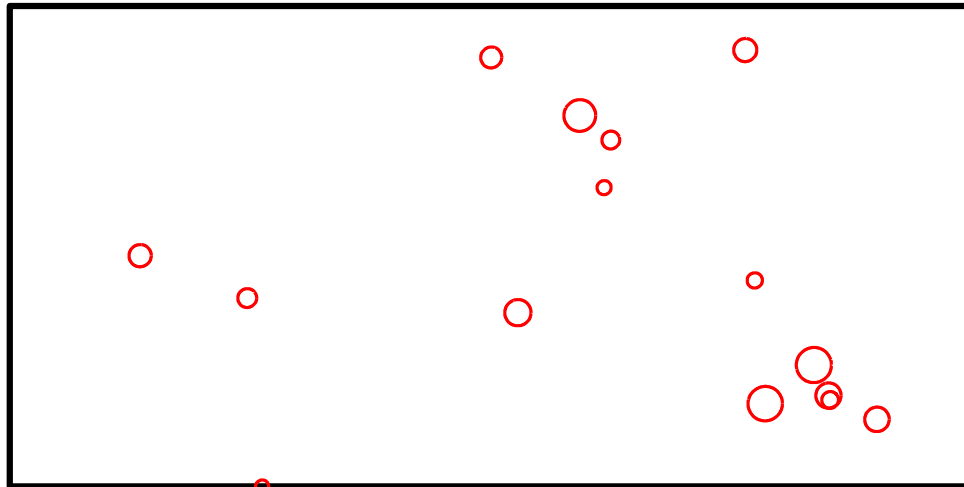


Figure 4: Map of tracks in aerogel tile 27. The diameter of the circles indicates the maximum diameter of the particle track in the aerogel, but is exaggerated by a factor of 10 in this figure. The aerogel tile measures $2\text{cm} \times 4\text{cm}$.

Clustering analysis of the Al foil crater data

Because of the limited statistics — due to small fluence — in some of the foils, 2PCF analysis was not appropriate for this dataset. Because detection thresholds among the various groups varied, we did not mix datasets from different groups when evaluating clustering.

We analyzed the spatial distribution of small craters using the same sum-inverse-square statistic $\hat{\zeta}$ that we used

for the analysis of tracks in individual aerogel tiles (Fig. 5). Out of eight scan regions on six foils, six showed significant ($> 2\sigma$) evidence for non-random spatial distributions.

During the course of surveying foil 8N, the Open University group discovered a spectacular cluster of 37 craters contained in an approximately $20\ \mu\text{m} \times 20\ \mu\text{m}$ area (Fig. 6). In this analysis, this cluster was counted as only one crater. If the components of the cluster been counted individually, the statistical significance for clustering would have been unmeasurably high ($\gg 5\sigma$) by Monte Carlo methods.

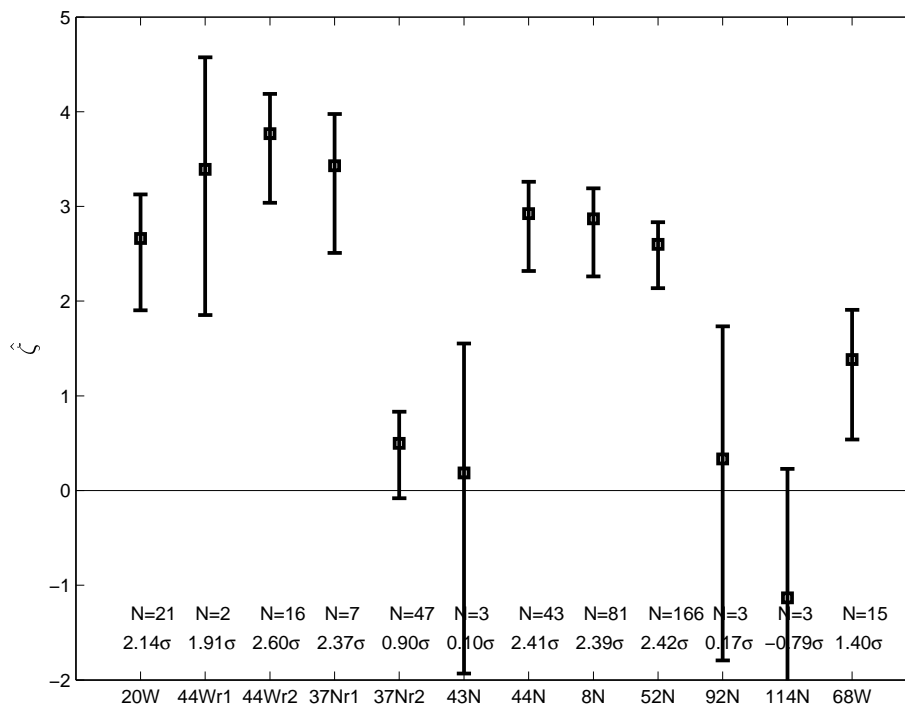


Figure 5: $\hat{\zeta}$ for eight foil surveys. A random distribution of crater positions corresponds to $\hat{\zeta} = 0$. The distributions are asymmetric and non-Gaussian, so the confidence level, expressed in units of σ , is listed for each foil. This crater cluster in 8N, shown in Fig. 6, was treated as one crater in this analysis. The suffixes “r1” and “r2” refer to different regions of the same foil.

Summary of clustering analysis

Small craters in the foils are clustered at a statistically significant level. 2PCF and $\hat{\zeta}$ analyses of the spatial distribution of tracks in aerogel also show evidence of weak clustering, although the statistical significance is somewhat smaller. The two analyses show different behaviors as a function of minimum aerogel track size. The 2PCF

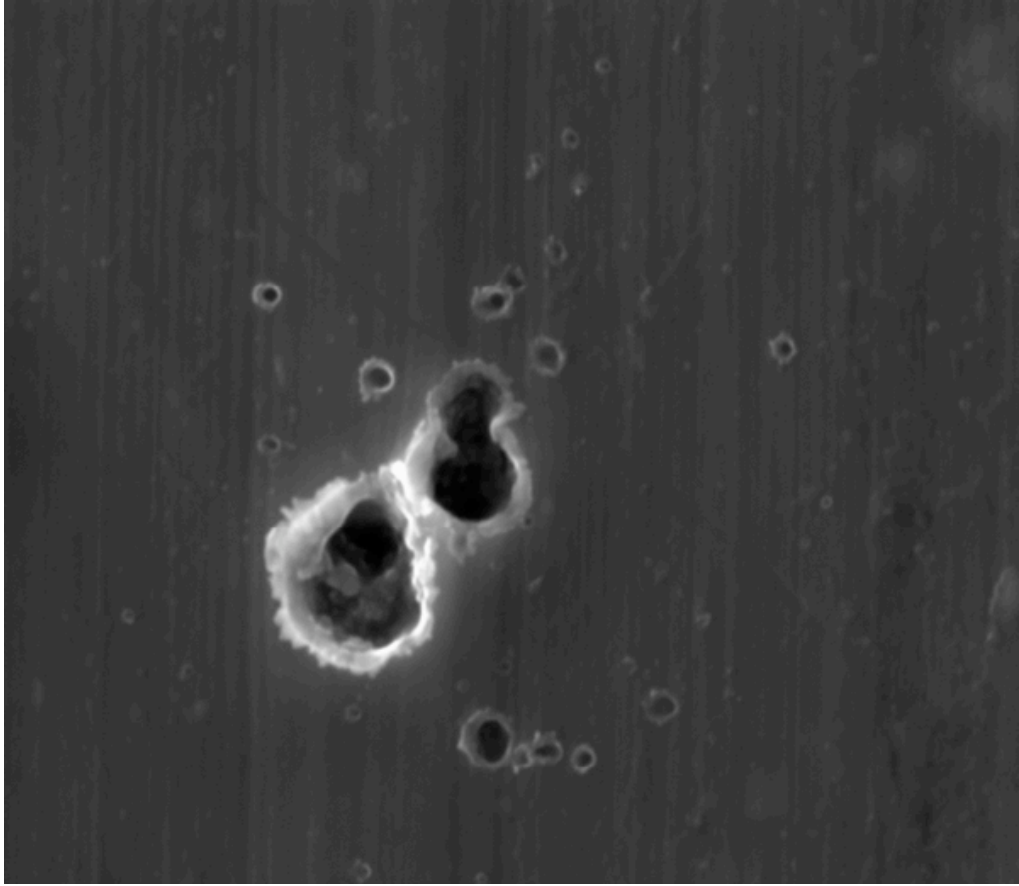


Figure 6: A cluster of 37 craters in foil 8N, discovered and imaged by the OU group. The craters are distributed over $350 \mu\text{m}^2$.

analysis indicates that $\sim 10\%$ of tracks are clustered.

2 Trajectory measurements of tracks in aerogel in five tiles

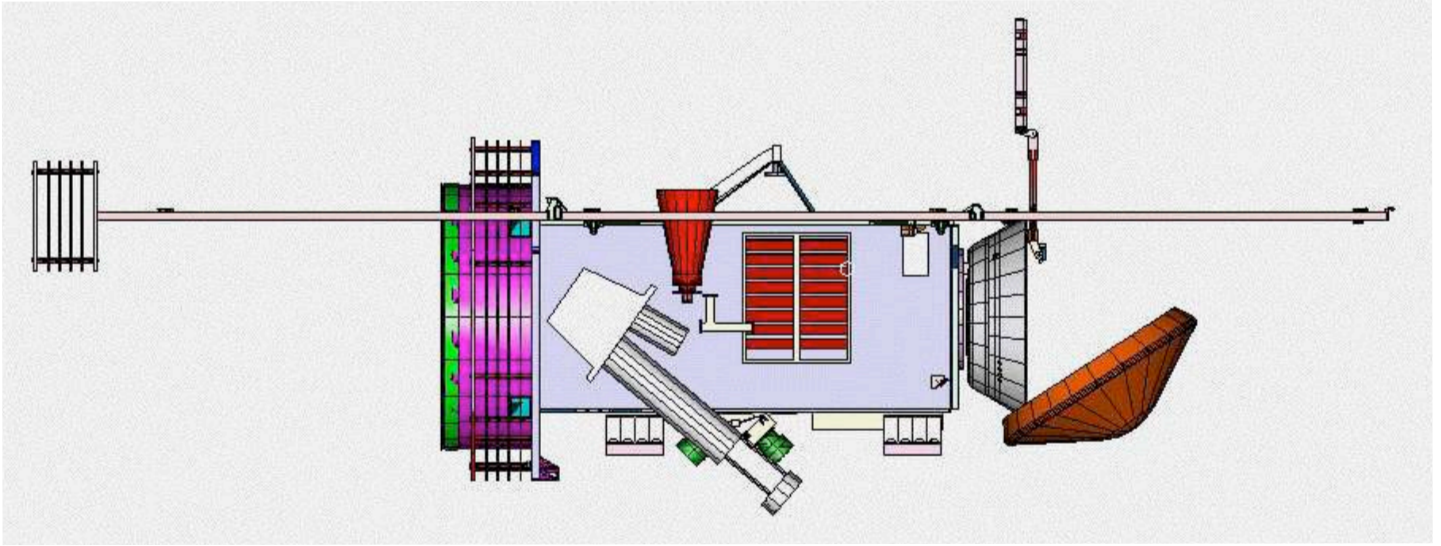
During our survey, we observed in tile 9 a large population of nearly parallel tracks that deviated significantly from normal incidence. We measured track trajectories (zenith and azimuth angles) for tracks in aerogel tiles 9, 38, 44, 52, and 86, using an optical microscope with an encoded stage ($0.5 \mu\text{m}$ resolution). We used a least-squares fit to estimate the trajectory of the tracks before impact with the aerogel. We excluded the bottom portions of tracks of terminal particles except on extremely small impacts ($< 200 \mu\text{m}$ deep). This was necessary because large hypervelocity particles often veer as they transition into the subsonic domain. So-called "whisker tracks", those with depths less than $\sim 200 \mu\text{m}$, were found to have correlated trajectories and were assumed therefore not to veer randomly from their initial trajectories prior to aerogel impact. Because the off-normal tracks were so numerous in tile 9, we did not select tracks randomly, but instead selected arbitrary regions and included all tracks within those regions.

In Fig. 7 we show a side view of the Stardust spacecraft. We projected the trajectories onto the plane of the central Whipple shield that protected the front of the spacecraft bus to evaluate the possibility that they may have originated from a collision between a cometary particle and the edge of the shield (Fig. 8). Of the tracks measured, 40 are consistent with primary, normal-incidence impacts, and 21 cross the plane of the Whipple shield at or below the bottom edge of the collector (below -20 cm). No projected trajectories crossed the plane of the Whipple shield above the projected top of the the collector.

The presence of a significant population of particles coming from below the bottom edge of the collector suggests the existence of secondary ejecta from the Whipple shield. However, we cannot exclude the possibility that the off-normal population is a population of dust with a large radial velocity component with respect to the Wild2 nucleus ($\sim 1 \text{ km sec}^{-1}$) that marginally misses the Whipple shield. We discuss this possibility further below.

In addition, several clusters of tracks had both high incidence angles and correlated trajectories. One of these clusters on tile 9 had four tracks within a 1 mm^2 area, and their trajectories projected toward the center edge of the Whipple shield. This suggests that particles with a high incidence angle are clustered.

We observed that off-normal tracks systematically exhibit a morphology distinct from the morphologies of



1

Figure 7: Side view of the Stardust spacecraft.

normal tracks. Off-normal tracks generally lack a distinct bulb (tracks of type “A” (?)), while normal-incidence tracks are highly variable. We did no systematic study of this phenomenon.

In the course of scanning tile 44, we also discovered a population of highly oblique tracks, $\sim 70^\circ$. Their trajectories are consistent with an origin in ejecta from an impact on the spacecraft bus just below and forward of the collecting tray.

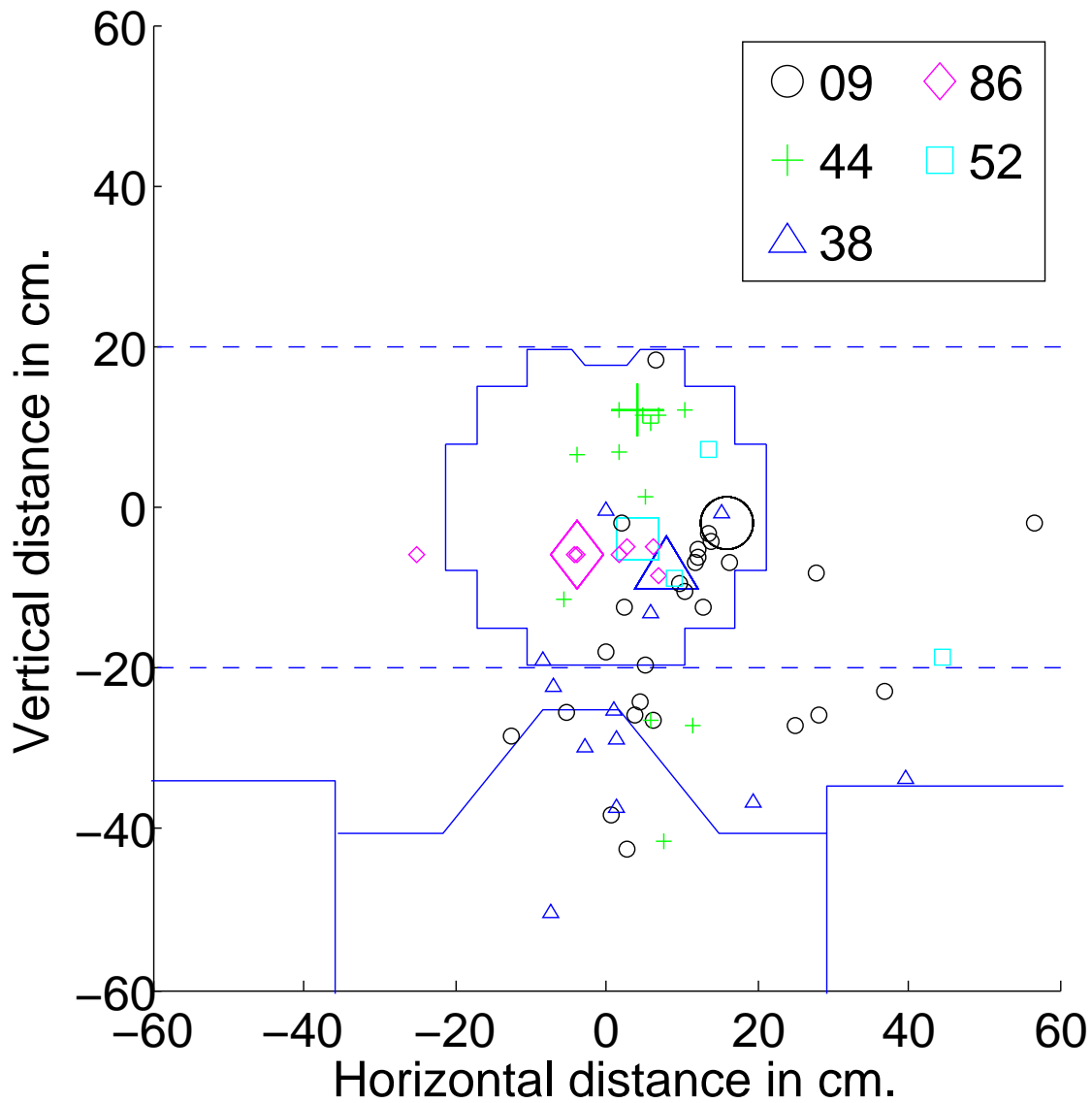


Figure 8: Aerogel tracks projected onto the plane of the central Whipple shield. The spacecraft bus is at the bottom of the picture. The Wild2 nucleus passed below the spacecraft. The Whipple shield outline is shown at -40 cm on the y axis and includes the trapezoidal protrusion. The rectangular Whipple shields to each side are the solar panel shields and are located in a different plane. Parallax between the solar Whipple shields and the impact sites has been ignored for readability. The outline of the collector is shown at the center. Symbols indicate the tile of origin; the tiles are the magnified symbols.

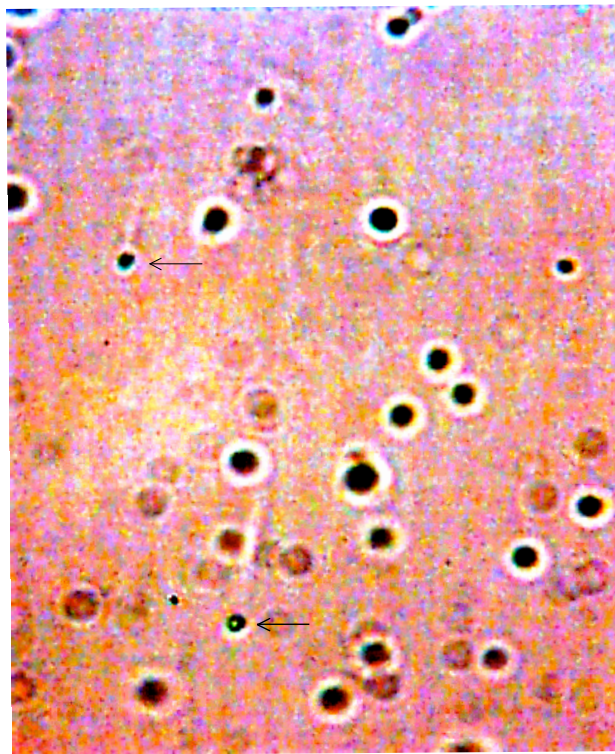


Figure 9: High-contrast image of highly-oblique secondary tracks. The field of view measures *** $40\ \mu$ by $60\ \mu$.

3 Crater and track residue compositions

Compositional Constraints: Detailed mineralogical and compositional analysis of numerous impactor residues in the interior of craters and tracks was conducted during Stardusts Preliminary Examination. None of them provided conclusive evidence that collisionally dislodged spacecraft materials contributed to the impact features seen on Stardusts cometary collector. Specifically, the cratering group (9) analyzed the melt residues of some 200 craters $< 5 \mu\text{m}$ in diameter via SEM-EDS methods, including features in exceptionally close proximity to each other that appeared to be part of a non-random impactor population. Also, some 38 individual craters composing the specific cluster illustrated in Fig. 6 were investigated by Bridges *et al.* (2007; in preparation), all yielding impactor residues consistent with cometary grains, and akin to those observed in the suite of 200 craters. Six large craters ($> 40 \mu\text{m}$) were analyzed in detail via SEM-EDS (Kearsley *et al.*, 2007) and TOF-SIMS (Leitner *et al.*, 2007), none yielding compositions compatible with spacecraft materials. Considering the ease with which natural and man-made impactors can be distinguished on space exposed surfaces retrieved from low Earth orbit (18), the Stardust crater observations suggest little to no collector contamination by spacecraft materials. It is noted, however, that the suite of $< 5 \mu\text{m}$ diameter craters included a few features ($< 2\%$) of indeterminate projectile composition; these features most likely contained residue masses below the detection threshold of the SEM-EDS method. It is possible also that they were produced by either aluminum or Kapton particles; Al impactors can obviously not be resolved from the Al-collector background, nor is the SEM-EDS method sensitive to small quantities of organic materials composed of low-Z elements. Analysis of numerous Stardust surfaces, however, does not reveal the presence of Kapton among the many organic contaminants, nor was Kapton observed in any of the tracks analyzed for organic components based on Sandford *et al.* (2006) (14). Additionally, a total of 27 tracks were analyzed via high-energy, synchrotron-produced, x-ray beams, yielding detailed elemental x-ray fluorescence maps of the impactor materials along the entire penetration path (15). These analyses illustrate distinctly lumpy distribution of elements, consistent with 1) the generation of numerous sub-micron particles as the impactor penetrates, and 2) the preservation of relatively large particles at the terminus of individual tracks. None of these individual particles, large or small, yields evidence for spacecraft derived origins. This is corroborated by quantitative TEM

investigations of some 300-400 individual particles in 52 individual Stardust tracks (Zolensky et al, 2006), all yielding predominantly natural comet-materials. However, some rare particles rich in Ti, Au and Zr were observed and their origin is currently unresolved; although they seem anthropogenic, they do not necessarily represent materials collisionally dislodged from some spacecraft surface, as none of them was detected as crater residue. They also seem too infrequent to be the main source of the common and numerous non-random impacts on the collector. In summary, detailed compositional analysis of Stardust craters and tracks provides no evidence for a prominent collisional environment by spacecraft debris.

4 Discrepancy between size distributions from DFMI and crater observations

Two measurements of the dust fluence and size-frequency distribution from the Stardust Wild2 encounter have been reported. The Dust Flux Monitor Instrument (DFMI) measured the masses of impacting cometary dust *in situ* during the cometary encounter, using a combination of PVDF thin film sensors (for diameters $a > \sim 3 \mu\text{m}$) and piezo-electric acoustic sensors (for $a > \sim 50 \mu\text{m}$) (5, 8). Hörz *et al.* reported dust fluence and size-frequency distributions as derived from measurements of individual crater diameters in the Stardust cometary-collector aluminum foils (?). The measurements are strongly inconsistent, both in absolute fluence and in their spectral mass index, α . The disagreement is in the PVDF data, which show $\alpha \sim -0.85$. The acoustic data, which agree in fluence with the foil data in the overlap region around grain radius of $50 \mu\text{m}$, have a lower average slope ($\alpha = -0.5$) and fluences that are exactly coincident with that derived from the large craters. Despite considerable effort, neither group has been able to identify any technical problem with either technique that resolves the discrepancy.

We point out that a scenario exists that could resolve the discrepancy. A population of small dust grains with a large radial velocity ($> 1.4 \text{ km sec}^{-1}$) with respect to the Wild2 nucleus would be detected by DFMI because of its position on the nose of the spacecraft. We discuss expected ejection velocities of cometary dust in section 5. But because of shadowing by the spacecraft bus, this population would pass over the collector, missing it entirely. A population of dust with a somewhat slower velocity, $\sim 1 \text{ km sec}^{-1}$, could be consistent with the off-normal tracks that we observe. However, this shadowing effect would not operate during the second dust collection period, $\sim 4000 \text{ km}$ downrange of the point of closest approach. We note that the discrepancy between foil and DFMI spectral indices is larger for the second collection period.

5 Discussion

We consider three general scenarios in seeking to understand the clustering observations: fragmentation processes in the cometary coma, spacecraft-induced fragmentation unrelated to impacts, and fragmentation due to one or more impacts on the spacecraft.

Processes in the cometary coma

It is natural to expect that, after they are ejected from the comet nucleus, cometary dust particles spontaneously fragment as they are heated by the sun and any remaining volatile “glue” holding them together sublimates away. Fragmentation of larger aggregates released from the Wild 2 nucleus was inferred to explain the highly variable fluxes detected on sub-km to km scales in the in-situ DFMI data (5, 8). A number of possible modes of fragmentation, physical mechanisms and observational evidence from other comets were discussed by Clark *et al.* (3).

Fragmentation of larger aggregates released from the Wild 2 nucleus was detected as relatively large-scale (sub-km to km) clustering (4). However, three especially tight clusters account for 33% of all counts observed during the flyby (5). For each of these, the counts were confined within a single 100 ms DFMI measurement interval, or straddling only two intervals, and with counts in the prior and subsequent measurement intervals 1 to 3 orders of magnitude lower. The first case was at +1.65 sec after closest approach. The other two occurred in the late event, ~600 sec after flyby. It cannot be excluded that these three extremely tight clusters actually arrived over an interval significantly smaller than one measurement interval. These could possibly have consisted of multiple subclusters within which the spatial separations between sequential particles were so small that two or more impact events would have been sensed as a single event due to pulse pile-up in the ~ few microseconds signal processing chain in the DFMI electronics system (?). Thus, these intense clusters of counts could account for an even larger fraction of all events measured by DFMI and the clusters could be more spatially confined than the DFMI data can demonstrate.

Dispersion speed of disintegrating dust

Disaggregation can be most straight-forwardly modeled as a gradual loss of material which is volatile under coma conditions of solar illumination and very low pressure. This material is a mixture. Water, CO₂, and numerous other condensates, including high-volatility organic materials, are well-known constituents of the gas phase of cometary comae. In porous aggregates, the sublimation process itself would only very gently separate the non-volatile grains, unless the volatiles are somehow confined such that they can build up pressure before release. Stiction by residual surface material and van der Waals forces would resist immediate disaggregation. However, separation forces have been identified that would promote subsequent breakup. These include centrifugal and electrostatic forces.

The separation between particles at the time of observation depends upon the time since separation and the energetics of the separation process itself. Many generations of breakup are implied by the shapes of the dust size distributions in comae (3), and some of the progeny particles may have separated only minutes before observation.

Rotation is inevitable for particles in space. Asymmetric loss of volatiles and solar radiation pressure on albedo variations are driving forces, but simple stochastic variations in solar wind can also induce the particles to tumble. This breakup can be gentle. For example, separation distances between sibling particles from a common 35 μm diameter progenitor will be less than 1 cm at 1000 sec after centrifugal breakup, if the progenitor tumbles at a period greater than 10 sec. Smaller particles will produce siblings with even lower separation velocities.

Dust particles ejected from the comet, even if they are initially electrically neutral, become charged to a potential of several volts magnitude through a variety of mechanisms, including photoejection of electrons by solar ultraviolet radiation and absorption of fast electrons in the surrounding plasma. For 1 μm particles at 1.8 AU, charging requires ~ 100 sec (22); the charging time decreases inversely with increasing particle size. After fragmentation, the daughter fragments repel each other by electrostatic repulsion. In Fig. 10 we show the asymptotic separation speed of the daughter fragments as a function of parent particle mass and splitting fraction. For parent particles 10 μm in size or smaller, asymptotic separation speeds are at least 1 cm sec^{-1} or faster. We assume that during fission, charge is partitioned between the daughter fragments in proportion to their surface area. Separation speeds could be significantly lower only if the partition of charge departs dramatically from this assumption. From

Fig. 2, we see the strongest evidence for clustering at distances less than 10 cm. For fissioning $\sim 20 \mu\text{m}$ dust, we estimate a separation speed of order 1 cm sec^{-1} , so for these dust particles dispersal must have started no more than 10 sec before collection.

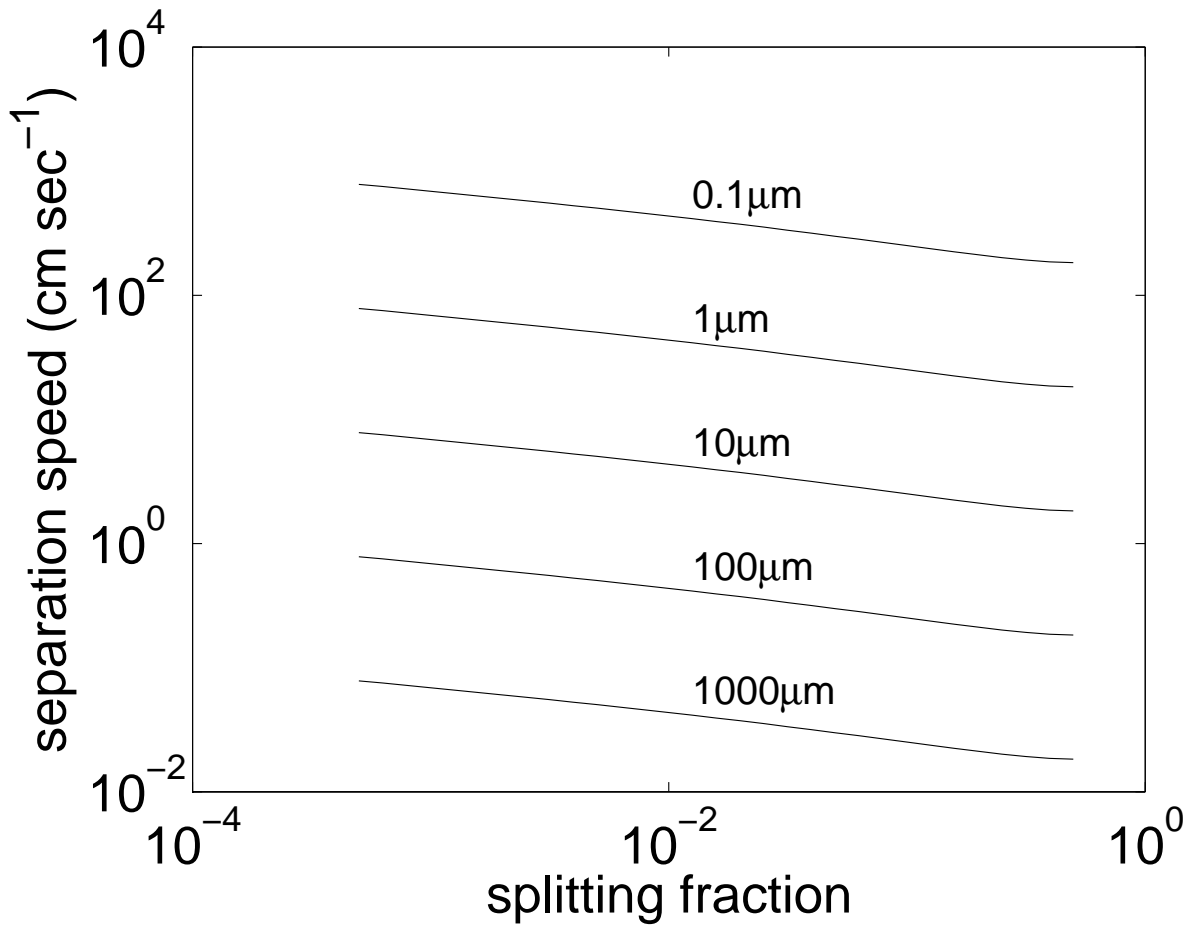


Figure 10: Separation velocity of fissioning dust particles with a potential of 1V, as a function of the fraction of the smaller daughter's mass compared with that of the parent. Each curve is labelled with the radius of the parent particle. Particles are assumed to be spheres with density 1.0 g cm^{-3} . Here we assume that during fission, charge is partitioned between the daughter fragments in proportion to their surface area. The separation velocity increases linearly with electric potential.

We define a parameter, η , which is the fraction of captured particles that belong to clusters with characteristic sizes of 10cm or smaller. From Fig. 2, $\eta \sim 0.1$. Following Clark *et al.* (3), we consider three principle

fragmentation modes: shedding, disintegration, and fission.

If particles principally fragment by shedding, in which numerous small particles are released gradually, a fraction η of the captured particles must have been shed within 10 sec of the collection time. If the shedding process occurs more or less continuously and smoothly, we then can estimate the characteristic shedding time as $\tau_s = 10 \text{ sec}/\eta \sim 100 \text{ sec}$. Similarly, if particles fragment by sudden and catastrophic disintegration, the characteristic disintegration time τ_d is of the same order. Dust particles must travel at least 236 km from the comet nucleus before capture by the spacecraft. This implies a speed significantly greater than 2 km sec^{-1} . We exclude this possibility for two reasons: first, as discussed previously, particles travelling radially outward from the comet nucleus at 2 km sec^{-1} would be geometrically prevented from reaching the collector over most of the first collection period and over all of the second. Second, it appears to be difficult to eject dust from the comet at such a large speed. At least some dust was probably ejected from Wild2 by entrainment in gas jets (12). The gas speed in these jets is unknown, but a strict upper limit can be calculated if it is assumed that these jets are supersonic, as would be the case if they were powered by a pressurized reservoir and there were constrictions near the comet surface (7). The limiting exit velocity of a supersonic nozzle with zero exit pressure is $\sqrt{2/(\gamma - 1)}c_s$, where γ is the ratio of specific heats and c_s is the sound speed. If the accelerating gas is diatomic, $\gamma = \frac{7}{5}$. The temperature of the comet is no more than room temperature, so the limiting gas speed is $\sim 0.7 \text{ km sec}^{-1}$. (We note that the limiting speed calculated by Yelle *et al.* (7), $\sim 3 \text{ km/sec}$, appears to be overestimated.) Acceleration of dust grains by an accelerating gas flow depends on the geometry of the exit channel, but is generally not very efficient at the expected pressures for grains larger than $\sim 1 \mu\text{m}$, so the asymptotic speed of the grains is a small fraction of the final gas velocity (7). So it appears that fragmentation principally by shedding or disintegration is not responsible for our observations of clustering.

Next we consider fission, in which particles fall apart stochastically into fragments of comparable size. The characteristic fission time, τ_f , is also of order 100 sec for the parents of the particles that were captured. If the progenitor object that was ejected from the comet had a mass m_0 and the characteristic mass of the captured particles was m_f , then the number of generations of fragmentation is $n_g \sim \log_2(m_0/m_f)$. For example, for

$m_0 = 1 \text{ g}$ and $m_f = 1 \text{ ng}$, $n_g \sim 30$. The required radial particle speed is reduced by a factor of n_g ; for a 1g progenitor, this is $\sim 70 \text{ m sec}^{-1}$. This is still an unexpectedly large escape speed for such a large object, but in this treatment we assumed that τ_f is a constant, independent of particle size. Although we cannot be quantitative, τ_f should increase dramatically with increasing particle size (3), this reduces the required radial particle speed accordingly.

Spacecraft-induced fragmentation (non-impact)

Did the particles fragment just before capture due to some influence of the spacecraft? We first consider the possibility of a gas-dynamic shock. From astronomical observations of Wild 2, the molecular production rate (23) was about $10^{28} \text{ molecules sec}^{-1}$. Gas should not come off any more slowly than the speed of sound, around 300 m sec^{-1} . By mass balance, the gas density at 236 km is about $< 4 \sim 10^7 \text{ cm}^{-3} (v/(300 \text{ m sec}^{-1}))$. The corresponding mean free path is $> 10 \text{ km}$, which is much larger than the spacecraft, so disruption by a gas-dynamic shock can be ruled out. Another possible source of gas is the spacecraft itself, especially from freshly activated surfaces due to sputtering by incoming particles. We currently have no basis for estimating the importance of spacecraft outgassing.

A charged dust grain will disintegrate if the electrostatic stress exceeds the tensile strength of the grain (24). While the tensile strength is independent of grain size, the electrostatic stress $\sim 1/a^2$, hence grains disrupt below a critical radius $a_\mu^c \approx \frac{7|\phi^V|}{\sqrt{F_T}}$, where a_μ^c is measured in μm , and F_T is the tensile strength, measured in dyne/cm^2 . Typical values for F_T range from 10^4 (dust ball) to 10^{11} (tektites), and it is thought to be on the order of 10^6 for fragile cometary dust particles. The expected floating potential in a cometary environment is a few volts positive. Grains smaller than 70–350 nm will break up, assuming a surface potential of 1–5 V. The products are even more unstable and continue disrupting until the field-emission limit is reached. Grains with $a_\mu \leq \phi^V/900$ lose their charge by emitting electrons and will not disrupt. This indicates that if electrostatic disruption is at work, the grouping of grains could be expected in the 1–5 nm range.

Even though electrostatic disruption is likely to take place, it is still difficult to see why these events would take place preferentially in the vicinity of the spacecraft. The close vicinity of the spacecraft is dominated by

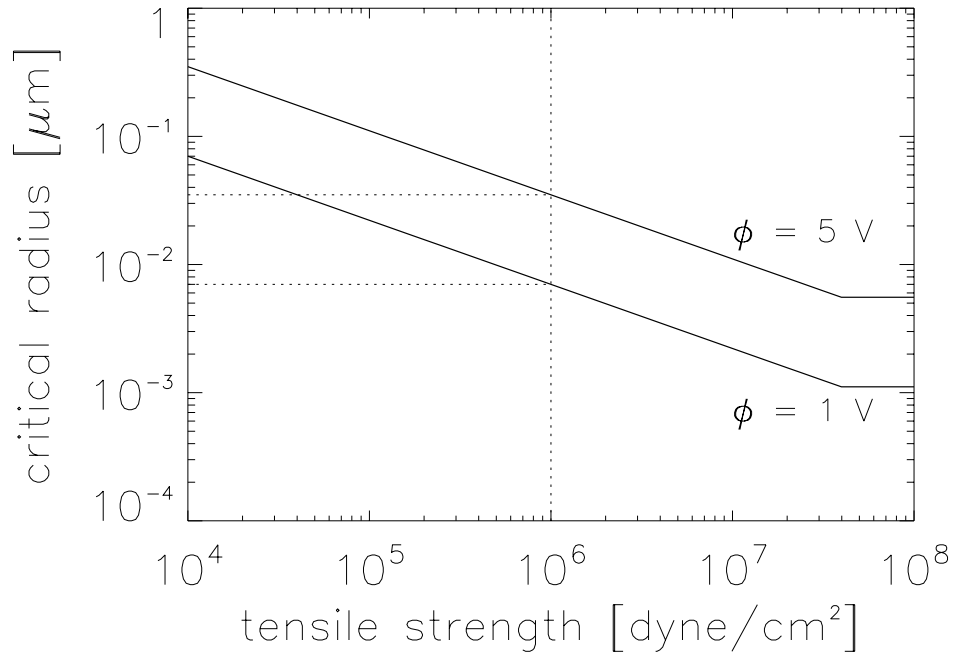


Figure 11: Critical radius of grains as function of the tensile strength. Grain smaller than the critical size are unstable against electrostatic disruption. The break is due to the field emission limit.

photoelectrons released from the lit side of the spacecraft, i.e., the side facing away from the nucleus. These photoelectrons have typical energies of 2 eV, so an approaching particle can only start losing its positive charge and — if big enough — can even switch to a negative charge, but just with a floating potential of about -2 V. The sign of the charge has no effect on the electrostatic stress ($\sim E^2$). The characteristic charges are expected to be comparable or smaller than the charges in the solar wind. Unless the charging/discharging itself would induce stresses, grains will not be exposed to a harsher electrostatic environment close to the spacecraft.

We have speculated that a large impact on one of the Whipple shields could have produced a cloud of particles, mostly fibers, that could serve as targets for cometary particles, fragmenting them just upstream of the collector. The time-averaged cross-section of these fibers upstream of the spacecraft is difficult to estimate. Large ejecta speeds ($\gg 10$ m sec $^{-1}$) are observed in test impacts on Whipple shields, so the loitering time of these fibers near the spacecraft is likely to be less than a second.

We consider the possibility that particles could form stable or quasi-stable configurations of spatially separated dust particles. Simpson, Simpson and Williams (20) have proposed that in some situations grains of different

sizes or of different compositions may charge to different signs. In this case, if smaller daughter fragments could quickly acquire a different charge sign than the larger parent after fragmentation, they could reconverge and rejoin the parent. They would then acquire the same charge as the parent by conduction, fragment again, and repeat this process indefinitely. However, the charging time of the smaller daughter fragment appears to be too long for this mechanism to be effective (22).

Spacecraft-induced fragmentation (impact)

Whipple shield as a target We now consider the probability that an impact on the central Whipple shield might produce secondary ejecta. These ejecta would appear in the collector as off-normal tracks. The Whipple shield consisted of polycyanate-carbon fiber face sheets with aluminum honeycomb between them, covered with a ceramic fabric (Nextel). This assembly was covered with aluminized polyimide kapton foil, ***xxx microns thick. There are two possible targets: the kapton rolled over the edge of the corner of the Whipple shield, and the kapton on the top surface of the Whipple shield.

An accurate estimate of the cross section of the rolled edge is probably impossible. If the radius of curvature of the foil as it folds around the edge is 1mm, then the total cross section is of order a few cm^2 , practically independent of spacecraft pitch. The fluence of particles greater than $10 \mu\text{m}$ in size as estimated from the crater data is $\sim 0.3 \text{ cm}^{-2}$ (9), so it is likely that at least one particle $> 10 \mu\text{m}$ in size impacted this rolled edge. The obliquity could vary from zero to 90 degrees depending on where the particle(s) hit on the curved surface of the roll.

The top face of the Whipple shield is another potential target. The obliquity of such impacts is likely to be very large — this depends on how taut the kapton was pulled during spacecraft construction. The extent to which wrinkles project above the projected edge of the Whipple shield is unknown. Shallow wrinkles are visible in documentary photographs. But even if the face had been perfectly flat, the cross section would be highly uncertain. If the spacecraft was slightly pitched up, the cross section would be zero. If the spacecraft was slightly pitched down, the cross section could be very large. For example, if the spacecraft was pitched down by even 1 degree, the cross section would be several times that of the front rolled edge.

Ejecta composition for high-obliquity impacts Most studies of high speed oblique impacts focus on the crater shape, rather than the ejected material. However, here what is of interest is the fate of the projectile material and any accompanying ejected target material which may depart from a primary impact site in front of the dust collector tray and which then hits the collector. General characteristics of the evolution of ejecta with increasing obliquity of impact are that the ejecta cloud begins to show asymmetries as the angle of incidence deviates from normal incidence. Further, at extreme angles of incidence the projectile no longer couples fully into the target during the impact, instead at the impact point an increasing fraction of it ricochets off the target. So-called impact decapitation can occur which causes the top of the projectile to shear off during impact and strike the target downstream of the primary crater (leading to secondary cratering), and at extreme angles significant fractions of the projectile ricochet off the surface altogether at some mean angle of rebound. This is in addition to any fine high speed spray produced during the initial contact stage of the impact. Thus what are essentially macroscopic fragments of the projectile survive the primary impact and travel away from the primary impact point. In addition, some of the material ejected from the target also travels in a forward direction, accompanying this projectile material.

This phenomenon has been reported in various experiments. Gault 1973 (29) reported on oblique impacts in dense crystalline rocks at speeds of around 1 to 8 km sec⁻¹. Although not reporting on the ejecta, the results showed that the displaced mass from the target varied with $\sin 2\theta$ (where θ is the angle of incidence measured from the target surface). Thus at very shallow angles of incidence, e.g. 10°, the displaced target mass was predicted to be only 3% of that at normal incidence. It should be noted however, that the data in that paper were at fixed angles of incidence, the lowest of which was 15°, with increments of 15° (i.e. 30° was the next lowest angle). There were considerable scatter on the data allowing some uncertainty as to the exact form of the θ dependence. Further, the work did not report on the fate of any projectile material. Nevertheless, the work strongly suggests that relatively little target material is ejected from shallow incidence impacts (even ignoring any asymmetries in direction of ejection). Impacts in dense crystalline rocks were revisited by amongst others, Burchell and Whitehorn 2003 (27). They used impacts speeds of 5–6 km sec⁻¹. and angles of incidence as low as 5°. This produced a different result, with a variation of ejected mass with angle of incidence which was linear in $\sin \theta$, although at shallow angles the

measured values were somewhat below this dependence. At 10° incidence their measured excavated crater mass was 10% of that at normal incidence, and at 5° it was 4%.

In a subsequent paper, Gault and Wedekind 1978 (11), studied oblique, high speed impacts in rock and particulate matter (quartz and pumice). For the non-cohesive quartz and pumice targets they reported that the excavated crater mass varied as $\sin \theta$. At very shallow angles (2°) craters were not only elongated but showed a distinct pattern as if of a chain of gradually smaller and slightly elongated circles one after the other on the surface (largest crater at main impact point). In this paper the ejecta were discussed. For shallow angle impacts on non-cohesive materials they observed the appearance of forbidden azimuthal zones in the ejecta distribution. These zones have bilateral symmetry, and extend both up and down-stream of the primary crater. They note that similar ejecta patterns are evident in large craters on the moon and planets. As well as the bulk ejecta from the target, Gault and Wedekind noted the presence of high speed ejecta which was impact melt and which was removed from the crater very early in the cratering process. At very shallow angles of incidence, this melt ejecta was confined to a very narrow range of azimuth angles in the downrange direction. The projectile material was also noted to undergo a concentration in the forward direction at shallow incidence. There was always some projectile material in the crater ejecta at all angles of incidence, but as the angle of incidence becomes shallower, there was increasing appearance and dominance of macroscopic projectile fragments in the forward ejecta.

There was no single critical angle for the onset of this focussing of the ejecta, it depends which phenomena were used to flag the on-set of ricochet reported by Gault and Wedekind 1978 (11). This was commented further on for example by Burchell and Mackay 1978 (26) who found several critical angles in oblique impacts, depending on whether crater shape, appearance of rays on the target surface etc. were used to flag the onset of this behaviour. Most authors note that these angles depend on target and projectile composition as well as impact speed, but that the phenomena of ricocheting projectile material in the forward direction is fully apparent for angles of incidence of 10° to 15° from the target surface. Indeed for very shallow angles (few degrees), at some speeds (still in excess of 1 km sec^{-1}) and some projectile/target materials the entire projectile can skip off the surface with little deformation and no apparent fragmentation. In such cases the forward ejecta mass is totally dominated by the projectile.

However, Gault and Wedekind 1978 (11) noted that (using non-cohesive targets) even where all large fragments in the downstream forward direction appeared to be projectile fragments, there was still a very fine sized population of target material. Looking at the angle of the ricocheting projectile fragments, Gault and Wedekind 1978 (11) found no simple angle of incidence equals angle of ricochet relationship. At 6.1 km sec^{-1} , they observed that for angles of incidence of $2^\circ - 7^\circ$, the ricochet angle was between 0.75° and 1.1° with the speed of the ricocheting fragments some 80 – 90% of the impact speed.

In Gault and Wedekind 1978 (11) no details were given of the amount of target material that was ejected during oblique impacts. Accordingly in a subsequent paper (Gault and Schultz 1986) (?) similar experiments on granular targets were repeated but with the addition that the history of target material was also considered (momentum transfer to the target and target material as ejecta). It was reported that for impacts at 7.5 the aluminium projectile fragmented with a mean velocity after ricochet of 82% of the pre-impact speed, and the projectile fragments were accompanied by target material of at least 27% of the projectile mass. In a later paper (Schultz and Gault 1990) (?) cumulative size distributions for the ejecta in oblique impacts are given from angles of incidence from 7.5° upward, but no directional information is given for the ejecta.

In recent years, as well as impacts on planetary scales, there has been interest in dust impacts on spacecraft surfaces in space (e.g. NASAs Long Duration Exposure Facility, or the Hubble Space Telescope and the European Space Agency's EuReCa spacecraft). This has been used to obtain estimates of dust fluxes in Low Earth Orbit for example. One problem that was reported however for both EuReCa and the HST, was that the solar cells which were the surfaces examined after retrieval from space, were found to contain clusters of hits, whose crater geometry suggested a common point source nearby. This was held to be primary impacts occurring on the body of the HST with the ejecta cloud then impacting the solar panel. A grazing incidence impact would produce a collimated cloud of ejecta, leading to the observed clustering on the solar panels, with an apparent common point source located nearby. A model for the ejecta was developed by Rival and Mandeville 1999 (36). The model was held to explain the observed distribution of clusters and oblong shaped (presumed oblique incidence) craters on the EuReCa solar panels, and to reconcile the flux at small particle sizes (where this effect will show up) with that

from other measurements (Drolshagen et al., 1996) (28).

Highly oblique incidence impacts in space have also been the subject of recent speculation as regards the loss of imaging capability on X-ray telescopes in Earth Orbit. These possess long mirrors which are highly inclined to the direction of the incidence radiation, this acts to focus the very short wavelength X-rays. It has been suggested, and backed up by laboratory studies, that these surfaces also act to focus ejecta from highly oblique dust impacts onto the CCD cameras. Laboratory tests of grazing incidence impacts on mirror surfaces (similar to the X-ray mirrors used in space in the XMM-Newton telescope) were made using iron projectiles (micron diameter) for angles of incidence at $1^\circ - 2^\circ$ and at speeds of $5.0 \pm 0.5 \text{ km sec}^{-1}$ (see Meidinger et al., 2003 (33)). The results produced ricochet of projectile material which impacted a secondary surface downstream of the primary impact site. SEM-EDS analysis of the craters (which ranged in size from 0.1 to 10 μm) showed only evidence for residues of the projectile and none from the mirror materials. The ricochet material had speeds almost equal to the incidence particles but their angle of ricochet from the surface was close to 0° , i.e. they were scattered very close to the target surface. Numerical simulations of these results were made by Palmieri et al., 2003 (34), and support the assumptions drawn from the experimental results. They note that the simulation results show that for incidence at 1° the projectile ricochets intact (albeit with some plastic deformation) but that as impact angle increases fragment of the ricocheting projectile occurs (at between 5° and 10°).

Recent developments in imaging have permitted real time images of ejecta clouds in 3 dimensions, including measuring particle velocity. This has been applied to oblique impacts in granular material at 30° incidence (Anderson et al., 2003) (25) and promises to be a powerful technique for future studies of ejecta in highly oblique impacts. It would be particularly interesting to apply it to impacts with very shallow angles of incidence.

Taking the above experimental reports as a whole, suggests that the amount of ejected material from a crater in a highly oblique impact is significantly less than from a normal incidence impact, but that it is still a finite fraction of the projectile mass. Furthermore, the projectile mass is itself ricocheting off the impact point, concentrated in a forward cone (raised above the target surface at a mean angle which may not be equal to the angle of incidence but is of similar magnitude) whereas the bulk of the ejected target material is directed into certain zones and avoids

others. The angle of the ricocheting material is not however, equal to the original incident angle of impact. The speed of the material is however, very close to that of the original particle.

Clustering of impacts on a secondary surface can also occur for normal incidence and penetration of thin targets. Studies of this often focus on penetration of thin metal sheets or shields (for a review see Kipp and Grady 1995) (?). Penetration of relatively thin sheets can produce fragmentation of the projectile and a cloud of projectile fragments and some material from the target then proceeds onwards in roughly the same direction as before. In Piekutowski 1995 (35) it is shown that this cloud has a central region of projectile fragments, with a front layer and rear shell of target fragments. In similar work, Schultz and Gault 1983;1985 (37, 38) fired Pyrex projectiles (diameter 6.1 cm, density 2.2 g/cc) at thin paper sheets at speeds of 4 to 6.4 km sec⁻¹. The impact velocity was not reduced by penetrating the paper, but the Pyrex projectiles were broken into many fragments. The cloud of fragments was initially smaller in diameter than the original particles, but developed laterally as it progressed beyond the front target. Subsequent impacts of such a cloud on granular targets produced broad, relatively shallow features of multiple overlapping pits or if there was greater dispersion of the cloud, a region of clustered but separate craters. It was assumed that the majority of the fragments in the clusters were disrupted projectile material.

To consider the fraction of a fragment cloud (after penetration of a thin sheet) which is projectile vs. target materials we make a simple model. We assume a sheet of Kapton extends laterally beyond the bumper shield and is hit by a particle at normal incidence. If the impacting particle has radius r , and the thin sheet thickness r/n , then an approximation can be made. At impact speeds above approximately 5 km sec⁻¹, and for n large (> 10), the hole in the target sheet will be approximately the cross-sectional area of the incidence particle. Ignoring any lips which occur on the target hole (which occur on both sides of the target sheet) and neglecting any ejecta on the front side of the target, the mass of displaced target material is given by $\pi(r/n)^2 \rho_t$, (area of hole multiplied by its thickness) compared to particle mass $4/3\pi r^3 \rho_p$, where ρ_t and ρ_p are respectively the target and projectile densities. The ratio of projectile to target masses in the cloud of ejecta beyond the target sheet is thus $4/3n\rho_p\rho_t$. If we assume the film is Kapton, then typical Kapton polyamide films have a density of 1.4 g/cc, and if we take an impactor as a typical silicate with density 2.4 g/cc, then for cases where n is 5 – 10, the mass of projectile in

the ejecta cloud will be 8 to 17 times that of the Kapton. Thus the projectile material may dominate the on-going cloud, but some Kapton will still be present. There may also be different size distributions for the two types of materials (Kapton and projectile).

Evidence for clustering of secondary craters in high speed impacts on Kapton is given by examination of impact craters on the Japanese Space Flyer Unit (SFU) which was retrieved from space and made available for laboratory study after 301 days in Low Earth Orbit in early 1996. An examination (Graham et al., 2003 (31)) of the multi layer insulation blankets on the SFU (with each layer in the blanket being made of Kapton, the thickest layer being the upper most layer which was $50\mu\text{m}$ thick) reported that small particle impact penetrations of the top layer of Kapton produced disruption of the impactor. There was then damage to subsequent layers and in lowermost layer of foil showing damage a cluster of pits was typically observed. Debris in these pits included projectile and melted Kapton from the foils above, however caution is required as it is not clear if this Kapton is from the front layer or as a result of lower speed penetration of the subsequent layers. With this caveat, it appears however that the shower of material from the penetration event consists of an intermingling of both projectile and Kapton fragments.

The reports of the composition of penetration clouds in impacts on metal sheets and those for impact damage to Kapton sheets, are consistent in that they predict a cloud of penetrating material which is a mixture of both projectile and target material. The data from the SFU show that, independent of the relative amounts of such materials, the target (Kapton) shows up as residue in subsequent impacts by the penetrating cloud. Since no Kapton residues are reported in the clusters on Stardust, it may be possible to rule out this method of producing clustering. However, there is no particular reason to expect *a priori* that the target material will have the same angular distribution as the projectile material. If the target material is scattered with a characteristic angular width that is m times that of the projectile material, then, if $m \ll 1$, then target material might not reach the collector at all because it is not sufficiently scattered. If $m \gg 1$ then the spatial density of the target material will be reduced with respect to that of the projectile material by $\sim m^2$. If $m \sim 10$, then the ratio goes from 8 – 17 to 800 – 1700. Since the foil would be accelerated from rest, it is likely that $m \gg 1$.

6 Summary

Here we summarize the observations, and review the evidence for and against all three scenarios that we have considered for explaining the impact clustering found on the Stardust aerogel and foil collectors.

Observations

1. There is statistically significant clustering of small tracks (maximum throat diameters $\sim 100 \mu\text{m}$) and small craters (maximum diameters $< 10 \mu\text{m}$) on all length scales from microns to tens of centimeters. The evidence for clustering among large tracks ($\gg 100 \mu\text{m}$) and craters ($> 10 \mu\text{m}$) is statistically significant but weaker.

2. We observe off-normal tracks in aerogel tiles, distributed among normal-incidence tracks. These tracks display a systematically different morphology than normal-incidence tracks.

3. We observe a divergence of off-normal tracks between tiles 9 (many tracks) and 44 (two tracks) consistent with an origin on the central Whipple shield. The distribution of the intersection of track trajectories with the plane of the Whipple shield shows many tracks below -20 cm and no tracks above $+20 \text{ cm}$. (0 cm is the projected center of the tray, and the positive direction is away from the spacecraft bus).

4. There is a large discrepancy in the spectral index and fluence at small particle sizes between the DFMI (PVDF detector) observations made during the cometary encounter and the crater observations made from the returned sample tray.

5. DFMI observed two periods of dust collection, centered on the closest approach time and another $\sim 4000 \text{ km}$ downrange of closest approach.

6. There is no evidence of spacecraft material in the impacts. It is not clear that this is a constraint, because of the relative lack of relevant experimental data on the presence of forward-scattered target material in highly oblique impacts of small friable projectiles.

7. Electrostatic repulsion sets a seemingly hard lower limit of $\gg 1 \text{ cm sec}^{-1}$ on the dispersion speed of disintegrating dust. This lower limit is based on straightforward physical principles.

Hypotheses

We have considered the following hypotheses:

- All impacts are primary, with a small radial velocity, and clustering occurs in the coma due to some unknown mechanism. This hypothesis is consistent with the observations of clustering and lack of spacecraft materials in impacts, but is not consistent with the presence of off-normal tracks, the expected large separation speeds expected for disintegrating dust in the cometary coma, nor the DFMI/crater discrepancy.

- All impacts are primary, with a large radial velocity, and clustering occurs in the coma due to some unknown mechanism. This hypothesis is consistent with the observations of clustering, lack of spacecraft materials in impacts, the presence of off-normal tracks, and could reconcile the DFMI data near closest approach with the cratering observations. This hypothesis is not consistent with the expected large separation speeds expected for disintegrating charged dust, nor with the DFMI data at 11 minutes after closest approach.

- Large impacts are primary, but there is a population of small grains due to at least one impact on the central Whipple shield. This appears to be consistent with all the observations, with the exception of the discrepancy between the cratering and DFMI measurements of dust fluences, the marginally significant clustering observed in both $\hat{\xi}_1$ and $\hat{\zeta}$ for large ($> 300 \mu\text{m}$) tracks, and (possibly) the lack of spacecraft materials in impacts.

Although no hypothesis explains all observations, we conclude that the preponderance of evidence points to an impact on the central Whipple shield as the origin of both off-normal tracks and clustering. To be sure, none of the scenarios have been completely ruled out — it is even possible that all three mechanisms operate. Nevertheless, it is clear that researchers should be aware of the possibility that tracks, particularly off-normal tracks, may have been “pre-processed” before capture by a collision with the central Whipple shield, and should be vigilant to contamination from the spacecraft.

7 Acknowledgments

We thank the entire Stardust Team — dedicated and talented people, too numerous to acknowledge individually here, whose intense effort over many years culminated in the successful recovery of the Stardust capsule in Jan-

uary 2006 bearing the first solid samples returned from beyond the Moon. We especially thank Steven Jones for synthesis of aerogel tiles.

AJW was supported by a NASA Stardust Participating Scientist grant. *** other acknowledgments here.

*** reorganize bibliography

References and Notes

1. Brownlee, stardust encounter reference
2. Davis and Peebles, *ApJ*, 267, 465, 1983
3. Clark, B. C. *et al.*, *JGR*, E12, 109, S03
4. Tsou et al *JGR* 2003
5. Tuzzolino, *Science*,...
6. Tuzzolino, *JGR* 108, 8115 (2003)
7. R. Yelle, et al.
8. Green et al. (*JGR* 109, E12S04, doi: 10/1029/2004JE002318, 2004).
9. Hörz et al science paper
10. N. Gehrels, *ApJ*, 303, 336 (1986).
11. D. E. Gault and J. A. Wedekind, *Proc. 9th Lunar Planet. Sci. Conf.*, 3843-3875 (1978).
12. Z. Sekanina, et al.
13. A. Kearsley, in preparation
14. S. Sandford, *Science*
15. G. Flynn, *Science*

16. J. Bridges, in preparation
17. J. Leitner et al., in preparation
18. Levine et al., LDEF, see Horz science paper
19. Horanyi & Goertz, ApJ 361, 155, 1990
20. Simpson, Simpson & Williams, Ap. Spa. Sci, 61,65 (1979)
21. S. W. Squyres, C. Howell, M. C. Liu & J. J. Lissauer, Icarus, 125, 67 (1997)
22. M. Horányi, Ann. Rev. Sci, **34**, 383 (1996)
23. Farnham and Schleicher, Icarus 173, 533 (2005)
24. D.A. Mendis and M. Rosenberg, Cosmic Dusty Plasma, Ann. Rev. Astron. Astrophys, 32, 419-463, 1994.
25. Anderson JLB, Schultz PH, Heineck JT. 2003. Asymmetry of ejecta flow during oblique impacts using three-dimensional particle image velocimetry. Journal of geophysical research-Planets 108 (E8), 5094.
26. Burchell M.J., and Mackay N. Crater Ellipticity in Hypervelocity Impact On Metals. J. of Geophys. Res. 103 E, 22761-22774.
27. Burchell M.J., and Whitehorn L. 2003. Oblique incidence hypervelocity impacts on rock. Monthly Notices of the Royal Astronomical Society 341, 192 -198.
28. Drolshagen G, McDonnell JAM, Stevenson TJ, Deshpande S, Kay L, Tanner WG, Mandeville JC, Carey WC, Maag CR, Griffiths AD, Shrine NG, Aceti R. 1996. Optical survey of micrometeoroid and space debris impact features on EURECA. Planetary and Space Science 44, 317 340.
29. Gault D.E. 1973. Displaced mass, depth, diameter, and effects of oblique trajectories for impact craters formed in dense crystalline rocks. The Moon 6, 32 44.

30. Gault D.E., and Schultz P.H. 1986. Oblique Impact: Projectile Ricochet, Concomitant Ejecta, and Momentum Transfer. *Meteoritics* 21, 368-369.
31. Graham G.A., Kearsley A.T., Wright I.P., Burchell M.J., and Taylor E.A. 2003. Observations on hypervelocity impact damage sustained by multi-layered insulation foils exposed in low earth orbit and simulated in the laboratory. *Int. J. Impact Engineering* 29, 307-316, 2003.
32. Kipp M.E., and Grady D.E. 1995. Experimental and Numerical Studies of High Velocity Impact Fragmentation. In *High Pressure Shock Compression of Solids II*. Eds. Davison L., Grady D.E., and Shahinpoor M. Pub. Springer. pp 283-339. ISBN 0-387-94402-8
33. Meidinger N., Aschenbach B., Brauninger H., Drolshagen G., Englhauser J., Hartmann R., Hartner G., Srama R., Struder L., Stubig M., and Trumper J. 2003. Experimental Verification of a Micrometeoroid Damage in the PN-CCD Camera System Aboard XMM-Newton. *X-ray and Gamma-ray Telescopes and Instruments for Astronomy, Proc. Of Society of Photo-optical Instrumentation Engineers (SPIE)* 4851, 243-254.
34. Palmieri D., Drolshagen G. and Lambert M. 2003. Numerical Simulation of Grazing Impacts from Micron Sized Particles on the XMM-Newton Mirrors. *International Journal of Impact Engineering* 29, 527-536.
35. Piekutowski A.J. 1995. Radiographic Studies of Impact Fragmentation. In *High Pressure Shock Compression of Solids II*. Eds. Davison L., Grady D.E., and Shahinpoor M. Pub. Springer. pp 150-175. ISBN 0-387-94402-8
36. Rival M., and Mandeville J.C. 1999. Modelling of Ejecta Produced Upon Hypervelocity Impacts. *Space Debris* 1, 45-57.
37. Schultz P.H., and Gault D.E. 1983. High velocity clustered impacts: Experiments and Implications. *Journal of Geophysical Research* 90(B5), 3701-3732.
38. Schultz P.H., and Gault D.E. 1983. Clustered impacts: Experimental results. *Lunar and Planetary Science Conference*, abstracts, page 674-674.

39. Schultz P.H., and Gault D.E. 1990. Prolonged global catastrophes from oblique impact. Geological Society of America Special Paper 247, pp 239 - 261.